

Neural Surface Reconstruction from Sparse Views Using Epipolar Geometry

Kaichen Zhou

University of Oxford

Abstract. This paper addresses the challenge of reconstructing surfaces from sparse view inputs, where ambiguity and occlusions due to missing information pose significant hurdles. We present a novel approach, named EpiS, that incorporates Epipolar information into the reconstruction process. Existing methods in sparse-view neural surface learning have mainly focused on mean and variance considerations using cost volumes for feature extraction. In contrast, our method aggregates coarse information from the cost volume into Epipolar features extracted from multiple source views, enabling the generation of fine-grained Signed Distance Function (SDF)-aware features. Additionally, we employ an attention mechanism along the line dimension to facilitate feature fusion based on the SDF feature. Furthermore, to address the information gaps in sparse conditions, we integrate depth information from monocular depth estimation using global and local regularization techniques. The global regularization utilizes a triplet loss function, while the local regularization employs a derivative loss function. Extensive experiments demonstrate that our approach outperforms state-of-the-art methods, especially in cases with sparse and generalizable conditions.

Keywords: Surface Reconstruction · Sparse Views · Generalizability

1 Introduction

Surface reconstruction from multi-view images is essential across various domains, including computer vision [5, 8, 46], robotics [54], and virtual reality [23, 53]. While multi-view stereo techniques are commonly used, past solutions relied on multi-step pipelines involving depth estimation, fusion, and meshing, leading to cumulative errors. Recently, there’s been a shift towards neural implicit representations for tasks like shape modeling and novel view synthesis. Methods like NeuS [42] and NeuS2 [44], inspired by NeRF [24], leverage volume rendering to represent 3D geometry using occupancy fields or Signed Distance Functions (SDF). However, they often suffer from subpar reconstruction quality due to limited geometry supervision. Attempts to enhance reconstruction quality involve integrating additional priors like sparse Structure-from-Motion (SfM) [37] point clouds or depth maps. Despite promising results, these methods face issues with lengthy per-scene optimization and struggle to generalize to new scenes. While recent SparseNeuS [20] has shown promise in generalizable implicit

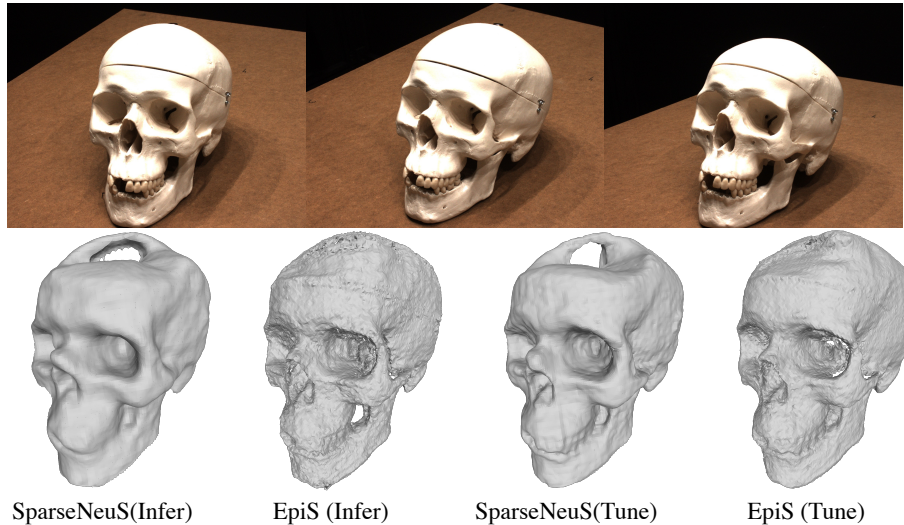


Fig. 1: Reconstruction results on the DTU dataset. Our approach has remarkable generalization capabilities across various scenes, successfully reconstructing neural surfaces using only three source images through fast network inference. Notably, the reconstruction quality of our fast inference process surpasses that of SparseNeuS, offering enhanced accuracy and fidelity. Additionally, our results can be further refined through per-scene adjustments. (All meshes are visualized with the help of MeshLab2022).

surface reconstruction, it faces resolution limitations due to memory constraints, resulting in over-smoothing of surfaces. Volrecon [36] enhances the performance of SparseNeuS [20], but it requires high-resolution ground truth depth maps for training, restricting its applicability to diverse scenarios.

Based on the concerns above, this paper presents EpiS, a swift and versatile surface reconstruction approach tailored for sparse view inputs. Unlike prior methods such as SparseNeuS [20] and GenS [31], which predominantly utilize the cost volume for feature extraction, EpiS leverages coarse information from the cost volume to guide the fusion of Epipolar features extracted from multiple source views, resulting in finely detailed SDF-aware features. Additionally, EpiS incorporates an attention mechanism to further fuse information along each target ray. Furthermore, to make up for the missing information under sparse views, EpiS makes use of the information generated from the pre-trained monocular depth model to regularize the learning process. Specifically, EpiS incorporates a global regularization by introducing a triplet loss function and a local regularization with the help of a partial derivative of a depth map. Our contributions can be summarized as follows:

- Our novel framework implements a coarse-fine strategy and integrates Epipolar information to achieve precise and adaptable surface reconstruction when dealing with sparse view input.

- We suggest incorporating a pre-trained model to supervise the inferred geometry information of the current model, achieved through both global triplet and local gradient regularizations.
- Extensive experimentation validates the accuracy of our proposed model in estimating geometry information, particularly in scenarios with sparse views and in generalizable task without the need for per-scene training as shown in Figure. 1.

2 Related Works

2.1 Multi-view depth estimation

Reconstructing 3D geometry from multi-view images poses a fundamental challenge in 3D vision, traditionally approached via depth-based or voxel-based methodologies. Multi-view stereo (MVS) methods, such as those by [3,9,39], rely on stereo correspondence for reconstructing depth maps. While early MVS methods utilized hand-crafted similarity metrics, recent advancements integrate deep learning for more precise matching. These approaches span volumetric [10,12,15], point cloud-based [7,16], and depth map-based methodologies [1,8,38,41,46]. Volumetric and point cloud-based techniques directly model objects but face memory limitations [3,39]. In contrast, depth map-based methods offer flexibility by separating depth map estimation and fusion, yielding commendable performance on diverse benchmarks [9]. However, their intricate processes, including depth filtering and fusion, may introduce cumulative errors. Despite recent strides in neural implicit representation, their performance trails behind state-of-the-art MVS methods. Addressing this gap, our paper introduces EpiS, showcasing superior performance compared to MVSNet [46] and COLMAP [37] under sparse view conditions through neural implicit representation.

2.2 Neural Implicit Surface Estimation

Neural implicit functions have recently gained traction as effective representations of 3D geometry [6,21,22,26,30,32] and appearance [18,19,25,28,33,40]. These functions are utilized in both surface and volume rendering approaches to realize 3D geometry reconstruction without the need for 3D supervision. While surface rendering [27,49,52] methods focus on single surface intersection points, volume rendering [29,42,48,51] considers multiple points along the ray, resulting in more impressive results. However, both approaches require expensive per-scene optimization and struggle to generalize to new scenes. Successful attempts at generalization [4,11,43,50], in novel view synthesis based on differentiable rendering have leveraged sparse views and radiance information. While these approaches yield more complete surfaces compared to traditional methods, they may struggle with complex structures and sharp corners.

In response to these concerns, recent research has aimed to enhance generalizability and accommodate sparse input by integrating traditional MVS techniques with differentiable rendering. SparseNeuS [20], for example, reconstructs

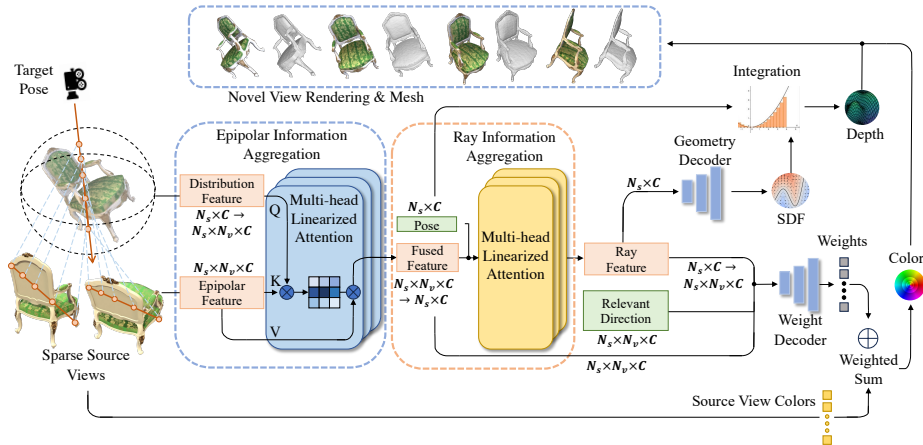


Fig. 2: Illustration of the Pipeline. Given a ray in the target view, it is projected onto source views to extract the epipolar feature and distribution feature (variance and mean) using a cost volume. Subsequently, the distribution features are utilized as queries, while the epipolar features serve as keys and values for cross-attention transformers, facilitating cross-view epipolar feature fusion. This fused feature set serves as input for subsequent ray transformers, enabling feature aggregation along the target ray. Finally, the resulting feature is used in the geometry MLP and weight decoder to predict corresponding signed distance functions (SDF) and multi-view color weights.

surfaces from nearby viewpoints but may lack detail and suffer from error accumulation. Furthermore, its two-stage training process prolongs training times and complexity. In contrast, VolRecon [36] and ReTR [17] rely on detailed depth ground truth for training, limiting their applicability and fine-tuning stability. Despite attempts at fine-tuning, their results remain inconsistent. Another recent approach, GenS [31], requires more views than the conventional sparse view setting to achieve comparable results.

This paper introduces EpiS, a method capable of achieving remarkable 3D reconstruction under conventional sparse view settings without requiring 3D ground truth supervision. Additionally, we propose efficient regularization techniques to ensure optimal fine-tuning performance using sparse view inputs as shown in Figure. 1.

3 Methodology

Given a set of images $\{I_i\}_{i=1}^n$ and their corresponding camera poses $\{P_i\}_{i=1}^n$, our objective is to design a model that can accurately estimate geometry information with these sparse inputs. This model also could achieve accurate surface estimation across different scenes without the need for per-scene optimization and can be further improved through our proposed fine-tuning strategies. (1) Existing research in sparse-view surface reconstruction, like SparseNeuS [20] and GenS [31], relies heavily on cost volumes for feature extraction and learning, which only considers their variances and means. Relying solely on variance and

means to characterize the distribution of multi-view information overlooks the intricate relationships between different views. To address this limitation, we propose a method that combines coarse information obtained from cost volumes with fine epipolar line information from multiple source views which enables a more precise estimation of surface information. Our approach utilizes an epipolar transformer to extract multi-view information and facilitate generalizable geometry information estimation across scenes.

(2) Furthermore, fine-tuning a model in a sparse setting presents unique challenges due to potential geometry ambiguity and occlusion arising from sparse view inputs. To address this, we propose introducing geometry regularization techniques. Additionally, pretrained large monocular depth models have demonstrated their effectiveness in estimating depth information accurately. Leveraging this capability, we introduce two fine-tuning regularization strategies aimed at improving depth estimation precision with sparse view inputs and leveraging estimated metric depth information.

3.1 Preliminaries

The goal of EpiS is to produce appearance and geometry information for a given novel view, following the pipeline established by NeuS [42].

Depth Information Estimation: This is realized by a network that takes a feature considering the 3D point position as input and predicts the surface information. The surface is represented by the zero-level set of the Signed Distance Function (SDF): $S = \{p \in \mathbb{R}^3 | \text{sdf}_\theta(p) = 0\}$. Following NeuS [42], we compute opaque density function $\rho(t)$ from S . To make the depth supervision differential, we could derive the rendered depth as in [54]:

$$\hat{D} = \sum_{j=1}^{N_S} T_j \alpha_j t_j, \quad T_j = \prod_{k=1}^{j-1} (1 - \alpha_k), \quad \alpha_j = 1 - \exp\left(-\int_{t_j}^{t_{j+1}} \rho(t) dt\right) \quad (1)$$

where t is the z value from the sampled point to the camera origin and N_S is number of sampled points along each ray.

Appearance Information Estimation: Following IBRNET [43], we make use of the color blending technique. Give a point p_t on the ray of a target frame, this point is projected into source frames to get the color information c_s of multiple pixels. A decoder would be used to predict the weights w_s of each source frame. Based on the volume rendering in NeRF [24], the final color is computed as:

$$\hat{C} = \sum_{j=1}^{N_S} T_j \alpha_j c_j, \quad c_j = \sum_{s=1}^{N_V} w_s * c_s, \quad (2)$$

where c_j is the predicted radiance and N_V is the number of source views.

3.2 Generalizable Framework

Cost Volume Construction To construct a cost volume for the target camera pose with N_V source frames, we first extract 2D feature maps $\{\mathbf{F}_i\}_{i=0}^{N_V}$ from the

input images $\{I_i\}_{i=0}^{N_V}$. Then, we construct a corresponding bounding box B for this target pose. To get the feature for each grid b in this bounding box. We project each grid on each source plane and get its feature $\{\mathbf{F}_i(P_i(b))\}_{i=0}^{N_V}$, where P_i is the transformation matrix between the target pose and the source pose. Following previous methods [46], we calculate the variance and mean of the projected features for each grid b of the bounding box to create a cost volume.

$$B_1(b) = \text{Var} \left(\mathbf{F}_i(P_i(b))_{i=1}^{N_V} \right), \quad B_2(b) = \text{Mean} \left(\mathbf{F}_i(P_i(b))_{i=1}^{N_V} \right), \quad (3)$$

Then, we employ a sparse 3D convolutional neural network Ψ to process the cost volume and get the coarse geometry aware feature volume \hat{B} .

Epipolar & Ray Information Aggregation Relying solely on variance and means to characterize the distribution of multi-view information overlooks the intricate relationships between multiple views. To address this limitation, we propose an approach that aggregates multi-view information along epipolar lines from multiple source views, while still considering distribution information.

Specifically, for each ray originating from a pixel, EpiS samples N_S points along the ray and projects them onto each source view. This process yields epipolar features from each source view. Subsequently, EpiS utilizes features from the cost volume as the query and the epipolar features from each source view as the key and value within a linearized attention mechanism [13]. This mechanism facilitates the fusion of multi-view epipolar information. Finally, a linear attention mechanism is employed to fuse information along the target ray.

(a) Epipolar Aggregation: This aggregation is realized through constructing a cross-attention transformer, as shown in Figure. 2. Given a ray $r_t = \{p_i\}_{i=1}^{i=N_S}$ from the sampled pixel of the target frame, EpiS extracts the corresponding feature $\mathbf{F}_B \in \mathbb{R}^{N_S \times C}$ from cost-volume \hat{B} and the multi-view epipolar feature $\mathbf{F}_E \in \mathbb{R}^{N_V \times N_S \times C}$ with the help of \mathbf{F}_i and P_i . EpiS initially applies corresponding matrices to process them and compute the query, key, and value as follows:

$$\mathbf{Q} = \mathbf{F}_B \mathbf{W}_Q, \mathbf{K} = \mathbf{F}_E \mathbf{W}_K, \mathbf{V} = \mathbf{F}_E \mathbf{W}_V, \quad \mathbf{W}_Q, \mathbf{W}_K, \mathbf{W}_V \in \mathbb{R}^{C \times C}. \quad (4)$$

Considering that the query, key, and value have different dimensions, EpiS repeats the query feature along the first dimension and we have $\mathbf{Q} \in \mathbb{R}^{N_S \times C} \rightarrow \mathbf{Q} \in \mathbb{R}^{N_V \times N_S \times C}$. To ensure Linearized Attention is applied across both multi-view and channel dimensions, we apply dimension permutation to the query, key, and value. In this way, we have $\mathbf{Q}, \mathbf{K}, \mathbf{V} \in \mathbb{R}^{N_S \times N_V \times C}$. These matrices are then split into h heads $\mathbf{Q} = \{\mathbf{Q}^i\}_{i=1}^h$, $\mathbf{K} = \{\mathbf{K}^i\}_{i=1}^h$, and $\mathbf{V} = \{\mathbf{V}^i\}_{i=1}^h$, each with $d = C/h$ channels. The cost-volume information is used to guide the learning process through the following Linearized Attention mechanism as:

$$\mathbf{X}_r^i = \frac{\phi(\mathbf{Q}_r^i)^T (\sum \phi(\mathbf{K}_r^i) (\mathbf{V}_r^i)^T)}{\phi(\mathbf{Q}_r^i)^T \sum \phi(\mathbf{K}_r^i)}, \quad (5)$$

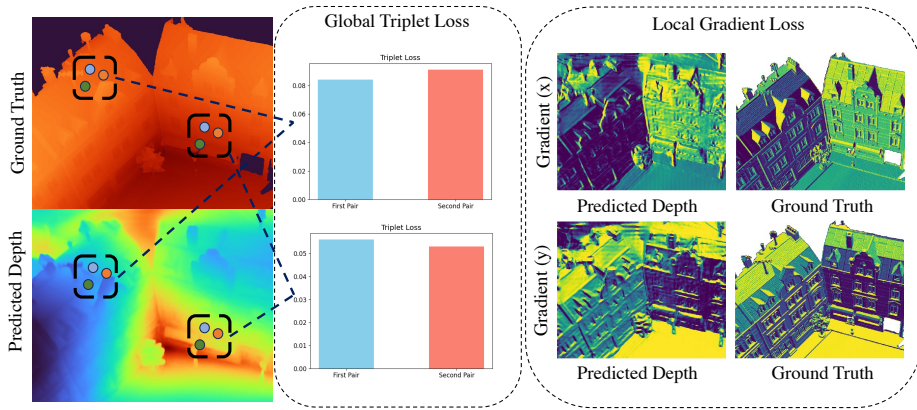


Fig. 3: Visualization of Our Fine-Tuning Strategy Designs. On the left, we present the predicted and ground truth depth maps. In the middle, we illustrate the triplet loss. On the right, we showcase the derivative gradients along the X and Y axes of the images.

where subscripting a matrix with i returns the i -th row along N_V dimension and $\phi(\cdot)$ is the kernel function. In our implementation, we use the same kernel function as in [13], which could be written as $\phi(\cdot) = \text{elu}(x) + 1$. Ultimately, we obtain fused feature $\mathbf{X} = \{\mathbf{X}^i\}_{i=1}^h \in \mathbb{R}^{N_S \times N_V \times C}$.

(b) Ray Aggregation: Efficient aggregation of epipolar information facilitates the integration of information from epipolar lines across various source views, as shown in Figure. 2. However, taking into account the feature of SDF, which is zero at the surface points and increases or decreases when away from the surface. We also need to consider the information along the ray. To realize this task, we first take the mean of \mathbf{X} along the N_V dimension and we have $\mathbf{X}' \in \mathbb{R}^{N_S \times C}$. Furthermore, given that N_S samples are randomly selected along each ray, the distance between each position is uncertain, particularly during the fine-sampling stage, as observed in NeRF [24]. To incorporate this information, we adopt the approach used in previous work, NeRF [24] to embed 3D position information as following $\text{emd}(\mathbf{x})$. We first concatenate this embedding information with feature information as $\hat{\mathbf{X}} = \text{concat}(\mathbf{X}', \text{emd}(\mathbf{x}))$. Finally following the previous section, we first process this feature with the help of linear mappings: $\hat{\mathbf{Q}} = \hat{\mathbf{X}}\hat{\mathbf{W}}_Q$, $\hat{\mathbf{K}} = \hat{\mathbf{X}}\hat{\mathbf{W}}_K$, $\hat{\mathbf{V}} = \hat{\mathbf{X}}\hat{\mathbf{W}}_V$. The final ray feature could be written as $\hat{\mathbf{X}} \in \mathbb{R}^{N_S \times C}$.

Geometry Decoder & Weights Decoder : To compute the final weights and Signed Distance Function (SDF), we employ a decoder, as shown in Figure. 2, similar to the approach used in NeuS [42]. Specifically, the Geometry Decoder f_θ utilizes the final ray feature $\hat{\mathbf{X}}$ as input to predict the final SDF. The decision not to include pose information as an input is because $\hat{\mathbf{X}}$ inherently encodes pose information. Additionally, the Weight Decoder takes the ray feature $\hat{\mathbf{X}}$,

fused feature \mathbf{X} , and relevant directional information as inputs to predict the final color weights.

3.3 Fine-Tuning Strategy for Accuracy

Pre-trained large-scale monocular depth estimation models, trained on extensive datasets, demonstrate efficiency in estimating depth across diverse scenarios [2, 35]. However, these models typically output depth information without scaling. While they perform well in estimating relative depth, absolute depth estimation can be challenging. Often, the generated depth lacks a scale factor and offset compared to the ground truth, as illustrated in DynPoint [55], where $d_{gt} = \alpha \hat{d} + \beta$. This feature complicates the use of generated depths for supervising depth estimation tasks. To address this, we propose both a global triplet loss function and a local gradient loss function.

(a) Global Triplet Loss: Addressing the challenge posed by the scale discrepancy between predicted depth and ground truth depth, directly employing predicted depth for supervision proves difficult. However, by capitalizing on the sampling of NR from the target frame during each iteration for training, exploiting the relative relationship between different rays becomes viable. Specifically, given sampled rays r_s , two rays r_1 and r_2 are randomly selected from NR . Subsequently, the global triplet loss function can be expressed as:

$$\mathcal{L}_{\text{global}} = \left((\hat{d}_1 - \hat{d}_s) \times (\tilde{d}_2 - \tilde{d}_s) - (\hat{d}_2 - \hat{d}_s) \times (\tilde{d}_1 - \tilde{d}_s) \right)^2, \quad (6)$$

where $\hat{d}_1, \hat{d}_2, \hat{d}_s$ represent the estimated depth by EpiS, and $\tilde{d}_1, \tilde{d}_2, \tilde{d}_s$ represent the estimated depth by the Pretrained Depth Model. Please note that while this loss function is named "global," it is applied only to local patches of the depth map. This approach is adopted because ensuring the relevance of the relationship between two distant pixels of the depth map cannot be guaranteed. The intuition of this loss function is demonstrated in the left part of Figure. 3.

(b) Local Gradient Loss: The global triplet loss primarily considers the overall structure of the depth map, often overlooking detailed local information. To incorporate local gradients, we utilize the partial derivatives of the depth map along the x and y axes. The partial derivative vectors are defined as $\hat{\mathbf{v}} = (\frac{\partial \hat{d}}{\partial x}, \frac{\partial \hat{d}}{\partial y})$ and $\tilde{\mathbf{v}} = (\frac{\partial \tilde{d}}{\partial x}, \frac{\partial \tilde{d}}{\partial y})$. The loss function could be written as:

$$\mathcal{L}_{\text{local}} = \left(1 - \frac{\hat{\mathbf{v}} \cdot \tilde{\mathbf{v}}}{\|\hat{\mathbf{v}}\| \cdot \|\tilde{\mathbf{v}}\|} \right)^2. \quad (7)$$

This loss function is employed to regularize the direction of the partial derivative vector while disregarding their absolute value. The intuition of this loss function is demonstrated in the right part of Figure. 3.

3.4 Loss Function

Given that EpiS relies solely on color information for supervising neural surface reconstruction, akin to prior neural surface reconstruction methods [44], we

Table 1: Quantitative results of sparse view reconstruction on 15 testing scenes from the DTU dataset. The upper part presents the performance of generalizable models, while the lower part displays the performance of fine-tuning models. If the result of EpiS outperforms all other methods, it will be **highlighted**. If the result of EpiS is the second best among all methods, it will be underlined.

| Method | 24 | 37 | 40 | 55 | 63 | 65 | 69 | 83 | 97 | 105 | 106 | 110 | 114 | 118 | 122 | Mean↓ |
|----------------------|-------------|-------------|-------------|-------------|-------------|-------------|-------------|-------------|-------------|-------------|-------------|-------------|-------------|-------------|-------------|-------------|
| PixelNerf [50] | 5.13 | 8.07 | 5.85 | 4.40 | 7.11 | 4.64 | 5.68 | 6.76 | 9.05 | 6.11 | 3.95 | 5.92 | 6.26 | 6.89 | 6.93 | 6.28 |
| IBRNet [43] | 2.29 | 3.70 | 2.66 | 1.83 | 3.02 | 2.83 | 1.77 | 2.28 | 2.73 | 1.96 | 1.87 | 2.13 | 1.58 | 2.05 | 2.09 | 2.32 |
| MVSNet [4] | 1.96 | 3.27 | 2.54 | 1.93 | 2.57 | 2.71 | 1.82 | 1.72 | 2.29 | 1.75 | 1.72 | 1.47 | 1.29 | 2.09 | 2.26 | 2.09 |
| SparseNeuS [20] | 1.68 | 3.06 | 2.25 | 1.10 | 2.37 | 2.18 | 1.28 | 1.47 | 1.80 | 1.23 | 1.19 | 1.17 | 0.75 | 1.56 | 1.55 | 1.64 |
| EpiS | 1.11 | 2.71 | 1.85 | <u>1.12</u> | 1.47 | 1.69 | <u>1.05</u> | 1.45 | 1.35 | 0.97 | <u>1.21</u> | <u>1.35</u> | 0.71 | 1.20 | 1.22 | 1.36 |
| UniSurf [29] | 5.08 | 7.18 | 3.96 | 5.30 | 4.61 | 2.24 | 3.94 | 3.14 | 5.63 | 3.40 | 5.09 | 6.38 | 2.98 | 4.05 | 2.81 | 4.39 |
| NeuS [42] | 4.57 | 4.49 | 3.97 | 4.32 | 4.63 | 1.95 | 4.68 | 3.83 | 4.15 | 2.50 | 1.52 | 6.47 | 1.26 | 5.57 | 6.11 | 4.00 |
| VolSDF [48] | 4.03 | 4.21 | 6.12 | 0.91 | 8.24 | 1.73 | 2.74 | 1.82 | 5.14 | 3.09 | 2.08 | 4.81 | 0.60 | 3.51 | 2.18 | 3.41 |
| IBRNet (ft) [43] | 1.67 | 2.97 | 2.26 | 1.56 | 2.52 | 2.30 | 1.50 | 2.05 | 2.02 | 1.73 | 1.66 | 1.63 | 1.17 | 1.84 | 1.61 | 1.90 |
| Colmap [37] | 0.90 | 2.89 | 1.63 | 1.08 | 2.18 | 1.94 | 1.61 | 1.30 | 2.34 | 1.28 | 1.10 | 1.42 | 0.76 | 1.17 | 1.14 | 1.52 |
| SparseNeuS (ft) [20] | 1.29 | 2.27 | 1.57 | 0.88 | 1.61 | 1.86 | 1.06 | 1.27 | 1.42 | 1.07 | 0.99 | 0.87 | 0.54 | 1.15 | 1.18 | 1.27 |
| MVSNet [46] | 1.05 | 2.52 | 1.71 | 1.04 | 1.45 | 1.52 | 0.88 | 1.29 | 1.38 | 1.05 | 0.91 | 0.66 | 0.61 | 1.08 | 1.16 | 1.22 |
| EpiS (ft) | <u>0.93</u> | 2.13 | 1.32 | 0.87 | 1.01 | 1.56 | 0.84 | 1.21 | 1.10 | 0.84 | 0.79 | <u>0.89</u> | 0.51 | 1.05 | 1.06 | 1.07 |

utilize the following loss functions for training:

$$\mathcal{L} = \mathcal{L}_{color} + \lambda_1 \mathcal{L}_{eik} + \lambda_2 \mathcal{L}_{sparse} + \lambda_3 \mathcal{L}_{global} + \lambda_4 \mathcal{L}_{local} \quad (8)$$

The first four loss functions are frequently employed in sparse view neural surface reconstruction tasks. The color loss function [44] is used to compute the distance between the predicted color from Eqn. 2, which could be written as:

$$\mathcal{L}_{color} = \frac{1}{\|\text{Patch}\|} \sum_{pix \in \text{Patch}} |\hat{c}(pix) - c(pix)|, \quad (9)$$

where Patch means the sampled patch used in one iteration and pix represents pixels within this patch.

The second Eikonal loss function [44] is used to regularize predicted SDF value predicted by our network, which could be written as:

$$\mathcal{L}_{eik} = \frac{1}{\|\mathbb{P}\|} \sum_{p \in \mathbb{P}} (\|\nabla \text{sdf}_\theta(p)\|_2 - 1)^2 \quad (10)$$

where \mathbb{P} is the set of all sampled points based on the sampled patch. This loss function forces network $\text{sdf}_\theta(p)$ to have a unit gradient.

To oversee the points beneath the predicted surface and prevent the occurrence of free surfaces, akin to [20], we integrate the sparse loss function term. This term aims to minimize the distance of points beneath the surface to zero as much as possible:

$$\mathcal{L}_{sparse} = \frac{1}{\|\mathbb{P}\|} \sum_{p \in \mathbb{P}} \exp(-\tau \cdot |\text{sdf}_\theta(p)|), \quad (11)$$

where τ is the hyperparameter.

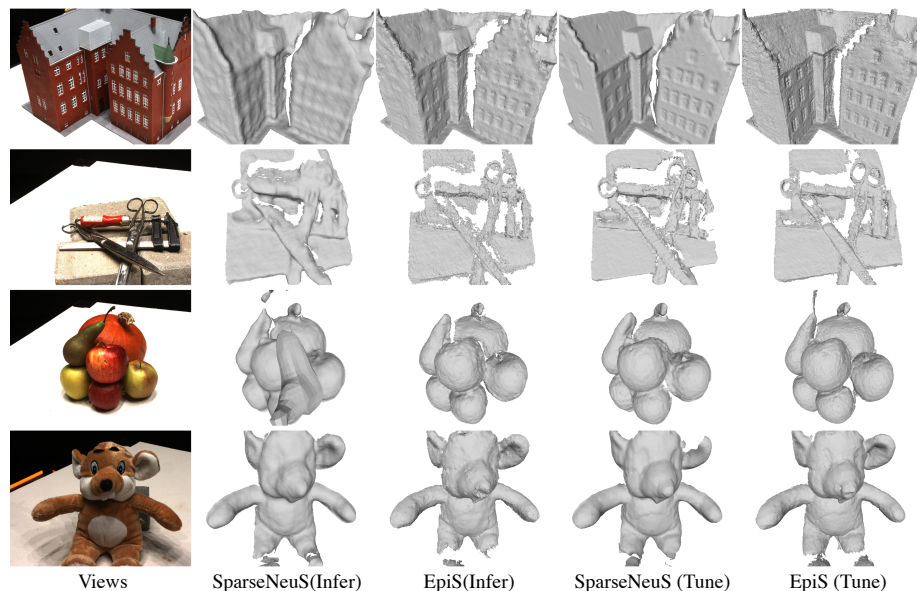


Fig. 4: Visualization results on the DTU dataset. EpiS produces precise outcomes without requiring fine-tuning. Moreover, fine-tuning further enhances the realism of our results, which is evident in the comparison.

4 Experiments

4.1 Experimental Settings

Baselines In our study, we follow the methodology outlined by MVSNet [4] for dense view analysis, utilizing the first 49 images for training. Our method undergoes comparison with state-of-the-art approaches from three classes: generic neural rendering methods, including PixelNerf [50], IBRNet [43], MVSNeRF [4] and SparseView [20]; per-scene optimization-based neural surfaces reconstruction methods like IDR [49], NeuS [44], VolSDF [48], and UniSurf [29]; and the classic MVS method COLMAP [37] and MVSNet [46]. All methods use three images as input. It’s worth noting that MVS methods, unlike neural implicit reconstruction, do not explicitly model scene parameters and cannot render novel views.

Besides, It’s worth noting that while GenS shows promising results, conducting a direct comparison poses challenges. The previous study [20] focused on utilizing three views ($N = 3$), while GenS [31] employs four views ($N = 4$), leading to significant differences in results. Moreover, the specific configuration of the four views used in GenS remains undisclosed, hindering clarity on their impact. Additionally, GenS’s use of 19 views for their Dense View experiment further complicates comparisons, especially considering the undisclosed rationale behind this choice. Due to these factors, we refrain from providing a direct comparison between EpiS and GenS.

Table 2: Depth evaluation on the DTU dataset. The result of mean absolute error (Abs.) is in millimeters. The results of threshold percentage ($< 1mm$, $< 2mm$, $< 4mm$) and mean absolute relative error (Rel.) are in percentage (%). If the result of EpiS outperforms all other methods, it will be **highlighted**. If the result of EpiS is the second best among all methods, it will be underlined.

| Method | Supervision | $< 1 \uparrow$ | $< 2 \uparrow$ | $< 4 \uparrow$ | Abs. \downarrow | Rel. \downarrow |
|-----------------|-------------|----------------|----------------|----------------|-------------------|-------------------|
| MVSNet [46] | RGBD | 29.95 | 52.82 | 72.33 | 13.62 | 1.67 |
| VolRecon [36] | RGBD | 44.22 | 65.62 | 80.19 | 7.87 | 1.00 |
| SparseNeuS [20] | RGB | 38.60 | 56.28 | 68.63 | 21.85 | 2.68 |
| EpiS | RGB | <u>43.97</u> | 66.16 | 83.33 | 7.79 | 0.99 |

Datasets We utilize the DTU dataset [1] for training, a multi-view stereo dataset comprising 124 scenes with ground truth point clouds and varying lighting conditions. Testing is conducted on the same 15 scenes as SparseNeuS, with the remaining scenes allocated for training. Depth maps rendered from the mesh serve as ground truth. Our framework, trained on the DTU dataset to ensure network generalization, employs 15 scenes for testing and the remaining 75 for training. Evaluation on testing scenes involves three views at 600×800 resolution, with each scene containing two sets of three images. Foreground masks provided by IDR are used for evaluation. To enhance memory efficiency during training, center-cropped images with 512×640 resolution are used. A simple threshold-based denoising strategy is applied to mitigate image noise. Additionally, we test our model on 7 challenging scenes from the BlendedMVS dataset [47], using one set of three images per scene with a resolution of 768×576 . It’s worth noting that in the per-scene fine-tuning stage, we optimize using the same three images without introducing new ones. Our experiments on both DTU and BlendedMVS datasets align with previous methods and include reporting Chamfer Distance for DTU and showcasing visual effects for BlendedMVS.

Implementation Our model, developed using PyTorch [34] and PyTorch Lightning, operates with an image resolution of 640×512 during training. Training occurs over 16 epochs, utilizing the Adam optimizer [14], on a single 4090 GPU with a learning rate of 10^{-4} . The batch size is set to 2, with 1024 rays sampled per batch. Both training and testing involve a hierarchical sampling strategy, initially sampling N coarse points uniformly on the ray and then employing importance sampling to sample additional N fine points on top of the coarse probability estimation, where $N_{coarse} = 64$ and $N_{fine} = 64$. The fine-level geometry encoding volumes are configured at a resolution of $96 \times 96 \times 96$. The sparse 3D CNN networks, structured akin to a U-Net, utilize a patch size of 5×5 for patch-based blending. During testing, the image resolution is adjusted to 800×600 .

4.2 Evaluation Results

Sparse View Reconstruction on DTU In the DTU dataset [1], we conduct sparse reconstruction using only 3 views, assessing performance through quan-

Table 3: Quantitative results of **dense view** reconstruction on 15 testing scenes of DTU dataset. If the result of EpiS outperforms all other methods, it will be **highlighted**. If the result of EpiS is the second best among all methods, it will be underlined.

| Method | 24 | 37 | 40 | 55 | 63 | 65 | 69 | 83 | 97 | 105 | 106 | 110 | 114 | 118 | 122 | Mean↓ |
|-------------|-------------|-------------|-------------|-------------|-------------|-------------|-------------|-------------|-------------|-------------|-------------|-------------|-------------|-------------|-------------|-------------|
| NeRF [24] | 1.90 | 1.60 | 1.85 | 0.58 | 2.28 | 1.27 | 1.47 | 1.67 | 2.05 | 1.07 | 0.88 | 2.53 | 1.06 | 1.15 | 0.96 | 1.49 |
| IDR [49] | 1.63 | 1.87 | 0.63 | 0.48 | 1.04 | 0.79 | 0.77 | 1.33 | 1.16 | 0.76 | 0.67 | 0.90 | 0.42 | 0.51 | 0.53 | 0.90 |
| MVSDF [52] | 0.83 | 1.76 | 0.88 | 0.44 | 1.11 | 0.90 | 0.75 | 1.26 | 1.02 | 1.35 | 0.87 | 0.84 | 0.34 | 0.47 | 0.46 | 0.88 |
| VolSDF [48] | 1.14 | 1.26 | 0.81 | 0.49 | 1.25 | 0.70 | 0.72 | 1.29 | 1.18 | 0.70 | 0.66 | 1.08 | 0.42 | 0.61 | 0.55 | 0.86 |
| NeuS [42] | 1.00 | 1.37 | 0.93 | 0.43 | 1.10 | 0.65 | 0.57 | 1.48 | 1.09 | 0.83 | 0.52 | 1.20 | 0.35 | 0.49 | 0.54 | 0.84 |
| Voxurf [45] | 0.65 | 0.74 | 0.39 | 0.35 | 0.96 | 0.64 | 0.85 | 1.58 | 1.01 | 0.68 | 0.60 | 1.11 | 0.37 | 0.45 | 0.47 | 0.72 |
| COLMAP [37] | 0.45 | 0.91 | 0.37 | 0.37 | 0.90 | 1.00 | 0.54 | 1.22 | 1.08 | 0.64 | 0.48 | 0.59 | 0.32 | 0.45 | 0.43 | 0.65 |
| EpiS | <u>0.51</u> | <u>0.81</u> | <u>0.42</u> | <u>0.44</u> | 0.82 | <u>0.67</u> | 0.54 | <u>1.24</u> | 0.95 | <u>0.70</u> | <u>0.54</u> | <u>0.66</u> | <u>0.38</u> | 0.44 | <u>0.44</u> | 0.63 |

titative measures like Chamfer Distances between predicted meshes and ground truth point clouds, as shown in Table. 1 In contrast to MVS methods such as COLMAP [37] and MVSNet [46], our approach exhibits approximately a 11% improvement over COLMAP, albeit slightly trailing behind MVSNet. It’s worth noting that MVSNet requires ground truth depth maps and lacks the capability to render novel views. Our method surpasses the state-of-the-art neural implicit reconstruction method SparseNeuS [20], achieving an 18% enhancement in the generalizable experiment and a 16% enhancement in the fine-tuning case. Moreover, our method outperforms VolRecon, which necessitates ground truth depth maps for training. Qualitative visualization in Figure. 4 highlights our method’s capacity to generate finer details and sharper boundaries than SparseNeuS.

Depth map evaluation on DTU In this experiment, we evaluate depth estimation performance using SparseNeuS [20] and MVSNet [46] across all views in each scan. For each reference view, we select the top 4 source views based on view selection scores from [46] for depth rendering. The results in Table. 2 indicate that our method outperforms both MVSNet and SparseNeuS across all metrics, and even surpasses VolRecon. This finding aligns with the results reported in Table. 1

Full View Reconstruction on DTU For a comprehensive comparison, we also conduct a mesh reconstruction experiment using dense views (the first 49 views for all scenarios). As demonstrated in Table. 3, our method consistently outperforms previous per-scene optimization methods and MVS methods without the need for further training.

Generalization on BlendedMVS To assess the generalization capability of our method, we extend our testing to BlendedMVS. The quantitative results are presented in Figure. 5. It is evident that EpiS exhibits superior performance in reconstructing details but may produce noisy boundaries compared to SparseNeuS.

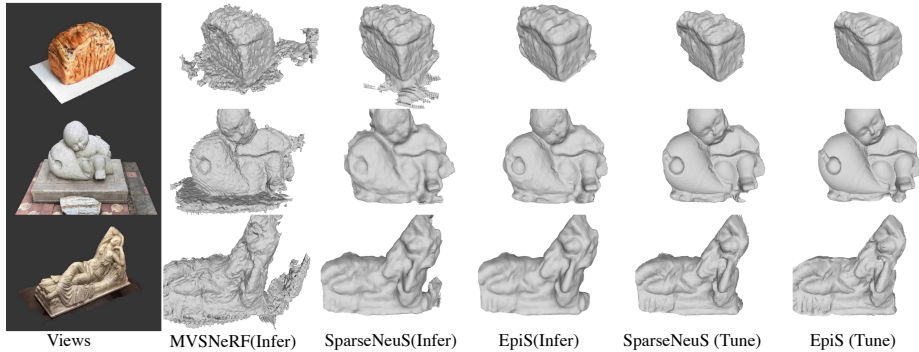


Fig. 5: Reconstruction results on the BlendedMVS dataset. EpiS yields reasonably accurate estimation even without pre-training on BlendedMVS. Fine-tuning enhances EpiS’s performance, leading to further improvements in accuracy.

4.3 Ablation Studies

In our ablation studies in Table. 4 on the DTU benchmark, we delve into the effectiveness of various components within our model. Table 4 provides a comprehensive summary of our findings across three key experiments: sparse view ($N = 3$) reconstruction, depth map evaluation, and full view reconstruction.

Epipolar Aggregation. In the first part of our ablation studies, we analyze the impact of removing the epipolar aggregation component from our framework. This adjustment results in the ray aggregation directly utilizing features from the cost-volume as input. The results in Table. 4 indicate that without epipolar aggregation, the ray aggregation process alone is insufficient to adequately capture the detailed geometry from the cost-volume data.

Global Triplet Loss. Moving on to the second part, we examine the consequences of eliminating the global triplet loss function, which plays a crucial role in supervising the rendered depth. Without this loss function, our model fails to effectively leverage the relevant depth relationships provided by the pre-trained large monocular depth model. As a result, there is a notable decline in performance.

Local Gradient Loss. In the third part of our ablation studies, we focus on the removal of the local gradient loss function, which also contributes to supervising the rendered depth. Without this loss function, our model experiences a further deterioration in performance, underscoring the critical role it plays in maintaining the accuracy of our results.

Number of Input Views. In the final segment of our ablation studies, we investigate the performance of EpiSs with varying numbers of input views. All

Table 4: Ablation studies of epipolar transformer, global depth loss, and local depth loss on the DTU dataset. We report results on both sparse view setting and dense view setting. If the result of EpiS outperforms all other methods, it will be **highlighted**. If the result of EpiS is the second best among all methods, it will be underlined.

| Method | Sparse View Recon. | Depth Map Eval. | | | | | Full View Recon. |
|--------------------------|--------------------|-----------------|--------------|--------------|--------------|-------------|------------------|
| | Chamfer↓ | < 1 ↑ | < 2 ↑ | < 4 ↑ | Abs.↓ | Rel. ↓ | Chamfer↓ |
| w/o Epipolar Aggregation | <u>1.70</u> | 31.04 | 67.19 | 82.55 | 08.03 | 1.10 | 0.71 |
| w/o Global Triplet Loss | 1.86 | 20.64 | 38.86 | 56.48 | 15.49 | 2.11 | 0.83 |
| w/o Local Gradient Loss | 1.90 | 15.84 | 33.65 | 54.72 | 18.93 | 3.72 | 0.98 |
| EpiS | 1.37 | 43.97 | 66.16 | 83.33 | 07.79 | 0.99 | 0.63 |

Table 5: Ablation study of the input view number on the DTU dataset. In this experiment, we modify the number of input views to test the performance of EpiS under different settings. If the result of EpiS outperforms all other methods, it will be **highlighted**. If the result of EpiS is the second best among all methods, it will be underlined.

| Method | Supervision | 2 Views | 3 Views | 4 Views | 6 Views |
|---------------|-------------|-------------|-------------|-------------|-------------|
| VolRecon [36] | RGBD | 1.72 | 1.38 | 1.35 | 1.33 |
| EpiS | RGB | 1.66 | 1.36 | 1.27 | 1.25 |

results are reported in Table. 5. Our findings reveal that increasing the number of input views significantly enhances the performance of EpiS. This improvement is attributed to the increased effectiveness in eliminating occlusion, particularly evident in sparse view scenarios. The addition of more views effectively mitigates occlusion challenges, consequently leading to notable enhancements in EpiS’s performance.

5 Conclusion

In this paper, we introduce EpiS, a generalizable method for sparse view neural surface reconstruction. Our approach incorporates an epipolar aggregation module to facilitate multi-view epipolar line fusion, guided by the cost volume. Additionally, we introduce a ray aggregation module to fuse information along the target ray. To regularize the depth learning process, we propose a global triplet loss and a local derivative loss, leveraging insights from a pretrained monocular depth model. Our model significantly outperforms state-of-the-art generalizable methods in neural surface reconstruction on the DTU dataset. Furthermore, the generalizability of our approach is demonstrated through compelling results on the BlendedMVS dataset.

References

1. Aanaes, H., Jensen, R.R., Vogiatzis, G., Tola, E., Dahl, A.B.: Large-scale data for multiple-view stereopsis. *International Journal of Computer Vision* **120**, 153–168 (2016) [3](#), [11](#)
2. Bhat, S.F., Birkl, R., Wofk, D., Wonka, P., Müller, M.: Zoedepth: Zero-shot transfer by combining relative and metric depth. *arXiv preprint arXiv:2302.12288* (2023) [8](#)
3. Campbell, N.D., Vogiatzis, G., Hernández, C., Cipolla, R.: Using multiple hypotheses to improve depth-maps for multi-view stereo. In: *Computer Vision—ECCV 2008: 10th European Conference on Computer Vision, Marseille, France, October 12–18, 2008, Proceedings, Part I 10*. pp. 766–779. Springer (2008) [3](#)
4. Chen, A., Xu, Z., Zhao, F., Zhang, X., Xiang, F., Yu, J., Su, H.: Mvsnerf: Fast generalizable radiance field reconstruction from multi-view stereo. In: *Proceedings of the IEEE/CVF International Conference on Computer Vision*. pp. 14124–14133 (2021) [3](#), [9](#), [10](#)
5. Ding, Y., Yuan, W., Zhu, Q., Zhang, H., Liu, X., Wang, Y., Liu, X.: Transmvsnet: Global context-aware multi-view stereo network with transformers. In: *Proceedings of the IEEE/CVF Conference on Computer Vision and Pattern Recognition*. pp. 8585–8594 (2022) [1](#)
6. Genova, K., Cole, F., Vlastic, D., Sarna, A., Freeman, W.T., Funkhouser, T.: Learning shape templates with structured implicit functions. In: *Proceedings of the IEEE/CVF International Conference on Computer Vision*. pp. 7154–7164 (2019) [3](#)
7. Gropp, A., Yariv, L., Haim, N., Atzmon, M., Lipman, Y.: Implicit geometric regularization for learning shapes. *arXiv preprint arXiv:2002.10099* (2020) [3](#)
8. Gu, X., Fan, Z., Zhu, S., Dai, Z., Tan, F., Tan, P.: Cascade cost volume for high-resolution multi-view stereo and stereo matching. In: *Proceedings of the IEEE/CVF conference on computer vision and pattern recognition*. pp. 2495–2504 (2020) [1](#), [3](#)
9. Ji, M., Gall, J., Zheng, H., Liu, Y., Fang, L.: Surfacenet: An end-to-end 3d neural network for multiview stereopsis. In: *Proceedings of the IEEE international conference on computer vision*. pp. 2307–2315 (2017) [3](#)
10. Ji, M., Zhang, J., Dai, Q., Fang, L.: Surfacenet+: An end-to-end 3d neural network for very sparse multi-view stereopsis. *IEEE Transactions on Pattern Analysis and Machine Intelligence* **43**(11), 4078–4093 (2020) [3](#)
11. Johari, M.M., Lepoittevin, Y., Fleuret, F.: Geonerf: Generalizing nerf with geometry priors. In: *Proceedings of the IEEE/CVF Conference on Computer Vision and Pattern Recognition*. pp. 18365–18375 (2022) [3](#)
12. Kar, A., Häne, C., Malik, J.: Learning a multi-view stereo machine. *Advances in neural information processing systems* **30** (2017) [3](#)
13. Katharopoulos, A., Vyas, A., Pappas, N., Fleuret, F.: Transformers are rnns: Fast autoregressive transformers with linear attention. In: *International conference on machine learning*. pp. 5156–5165. PMLR (2020) [6](#), [7](#)
14. Kingma, D.P., Ba, J.: Adam: A method for stochastic optimization. *arXiv preprint arXiv:1412.6980* (2014) [11](#)
15. Kutulakos, K.N., Seitz, S.M.: A theory of shape by space carving. *International journal of computer vision* **38**, 199–218 (2000) [3](#)
16. Lhuillier, M., Quan, L.: A quasi-dense approach to surface reconstruction from uncalibrated images. *IEEE transactions on pattern analysis and machine intelligence* **27**(3), 418–433 (2005) [3](#)

17. Liang, Y., He, H., Chen, Y.: Retr: Modeling rendering via transformer for generalizable neural surface reconstruction. *Advances in Neural Information Processing Systems* **36** (2024) [4](#)
18. Liu, L., Gu, J., Zaw Lin, K., Chua, T.S., Theobalt, C.: Neural sparse voxel fields. *Advances in Neural Information Processing Systems* **33**, 15651–15663 (2020) [3](#)
19. Liu, S., Zhang, Y., Peng, S., Shi, B., Pollefeys, M., Cui, Z.: Dist: Rendering deep implicit signed distance function with differentiable sphere tracing. In: *Proceedings of the IEEE/CVF Conference on Computer Vision and Pattern Recognition*. pp. 2019–2028 (2020) [3](#)
20. Long, X., Lin, C., Wang, P., Komura, T., Wang, W.: Sparseneus: Fast generalizable neural surface reconstruction from sparse views. In: *European Conference on Computer Vision*. pp. 210–227. Springer (2022) [1](#), [2](#), [3](#), [4](#), [9](#), [10](#), [11](#), [12](#)
21. Mescheder, L., Oechsle, M., Niemeyer, M., Nowozin, S., Geiger, A.: Occupancy networks: Learning 3d reconstruction in function space. In: *Proceedings of the IEEE/CVF conference on computer vision and pattern recognition*. pp. 4460–4470 (2019) [3](#)
22. Michalkiewicz, M., Pontes, J.K., Jack, D., Baktashmotlagh, M., Eriksson, A.: Implicit surface representations as layers in neural networks. In: *Proceedings of the IEEE/CVF International Conference on Computer Vision*. pp. 4743–4752 (2019) [3](#)
23. Middelberg, S., Sattler, T., Untzelmann, O., Kobbelt, L.: Scalable 6-dof localization on mobile devices. In: *Computer Vision—ECCV 2014: 13th European Conference, Zurich, Switzerland, September 6–12, 2014, Proceedings, Part II 13*. pp. 268–283. Springer (2014) [1](#)
24. Mildenhall, B., Srinivasan, P.P., Tanck, M., Barron, J.T., Ramamoorthi, R., Ng, R.: Nerf: Representing scenes as neural radiance fields for view synthesis. *Communications of the ACM* **65**(1), 99–106 (2021) [1](#), [5](#), [7](#), [12](#)
25. Müller, T., Evans, A., Schied, C., Keller, A.: Instant neural graphics primitives with a multiresolution hash encoding. *ACM Transactions on Graphics (ToG)* **41**(4), 1–15 (2022) [3](#)
26. Niemeyer, M., Mescheder, L., Oechsle, M., Geiger, A.: Occupancy flow: 4d reconstruction by learning particle dynamics. In: *Proceedings of the IEEE/CVF international conference on computer vision*. pp. 5379–5389 (2019) [3](#)
27. Niemeyer, M., Mescheder, L., Oechsle, M., Geiger, A.: Differentiable volumetric rendering: Learning implicit 3d representations without 3d supervision. In: *Proceedings of the IEEE/CVF Conference on Computer Vision and Pattern Recognition*. pp. 3504–3515 (2020) [3](#)
28. Oechsle, M., Mescheder, L., Niemeyer, M., Strauss, T., Geiger, A.: Texture fields: Learning texture representations in function space. In: *Proceedings of the IEEE/CVF International Conference on Computer Vision*. pp. 4531–4540 (2019) [3](#)
29. Oechsle, M., Peng, S., Geiger, A.: Unisurf: Unifying neural implicit surfaces and radiance fields for multi-view reconstruction. In: *Proceedings of the IEEE/CVF International Conference on Computer Vision*. pp. 5589–5599 (2021) [3](#), [9](#), [10](#)
30. Park, J.J., Florence, P., Straub, J., Newcombe, R., Lovegrove, S.: DeepSDF: Learning continuous signed distance functions for shape representation. In: *Proceedings of the IEEE/CVF conference on computer vision and pattern recognition*. pp. 165–174 (2019) [3](#)
31. Peng, R., Gu, X., Tang, L., Shen, S., Yu, F., Wang, R.: Gens: Generalizable neural surface reconstruction from multi-view images. *Advances in Neural Information Processing Systems* **36** (2024) [2](#), [4](#), [10](#)

32. Peng, S., Niemeyer, M., Mescheder, L., Pollefeys, M., Geiger, A.: Convolutional occupancy networks. In: *Computer Vision–ECCV 2020: 16th European Conference, Glasgow, UK, August 23–28, 2020, Proceedings, Part III* 16. pp. 523–540. Springer (2020) [3](#)
33. Pumarola, A., Corona, E., Pons-Moll, G., Moreno-Noguer, F.: D-nerf: Neural radiance fields for dynamic scenes. In: *Proceedings of the IEEE/CVF Conference on Computer Vision and Pattern Recognition*. pp. 10318–10327 (2021) [3](#)
34. Pytorch, A.D.I.: Pytorch (2018) [11](#)
35. Ranftl, R., Lasinger, K., Hafner, D., Schindler, K., Koltun, V.: Towards robust monocular depth estimation: Mixing datasets for zero-shot cross-dataset transfer. *IEEE transactions on pattern analysis and machine intelligence* **44**(3), 1623–1637 (2020) [8](#)
36. Ren, Y., Zhang, T., Pollefeys, M., Süssstrunk, S., Wang, F.: Volrecon: Volume rendering of signed ray distance functions for generalizable multi-view reconstruction. In: *Proceedings of the IEEE/CVF Conference on Computer Vision and Pattern Recognition*. pp. 16685–16695 (2023) [2](#), [4](#), [11](#), [14](#)
37. Schonberger, J.L., Frahm, J.M.: Structure-from-motion revisited. In: *Proceedings of the IEEE conference on computer vision and pattern recognition*. pp. 4104–4113 (2016) [1](#), [3](#), [9](#), [10](#), [12](#)
38. Schönberger, J.L., Zheng, E., Frahm, J.M., Pollefeys, M.: Pixelwise view selection for unstructured multi-view stereo. In: *Computer Vision–ECCV 2016: 14th European Conference, Amsterdam, The Netherlands, October 11–14, 2016, Proceedings, Part III* 14. pp. 501–518. Springer (2016) [3](#)
39. Stereopsis, R.M.: Accurate, dense, and robust multiview stereopsis. *IEEE TRANSACTIONS ON PATTERN ANALYSIS AND MACHINE INTELLIGENCE* **32**(8) (2010) [3](#)
40. Sun, C., Sun, M., Chen, H.T.: Direct voxel grid optimization: Super-fast convergence for radiance fields reconstruction. In: *Proceedings of the IEEE/CVF Conference on Computer Vision and Pattern Recognition*. pp. 5459–5469 (2022) [3](#)
41. Tola, E., Strecha, C., Fua, P.: Efficient large-scale multi-view stereo for ultra high-resolution image sets. *Machine Vision and Applications* **23**, 903–920 (2012) [3](#)
42. Wang, P., Liu, L., Liu, Y., Theobalt, C., Komura, T., Wang, W.: Neus: Learning neural implicit surfaces by volume rendering for multi-view reconstruction. *arXiv preprint arXiv:2106.10689* (2021) [1](#), [3](#), [5](#), [7](#), [9](#), [12](#)
43. Wang, Q., Wang, Z., Genova, K., Srinivasan, P.P., Zhou, H., Barron, J.T., Martin-Brualla, R., Snavely, N., Funkhouser, T.: Ibrnet: Learning multi-view image-based rendering. In: *Proceedings of the IEEE/CVF Conference on Computer Vision and Pattern Recognition*. pp. 4690–4699 (2021) [3](#), [5](#), [9](#), [10](#)
44. Wang, Y., Han, Q., Habermann, M., Daniilidis, K., Theobalt, C., Liu, L.: Neus2: Fast learning of neural implicit surfaces for multi-view reconstruction. In: *Proceedings of the IEEE/CVF International Conference on Computer Vision*. pp. 3295–3306 (2023) [1](#), [8](#), [9](#), [10](#)
45. Wu, T., Wang, J., Pan, X., Xu, X., Theobalt, C., Liu, Z., Lin, D.: Voxurf: Voxel-based efficient and accurate neural surface reconstruction. In: *International Conference on Learning Representations (ICLR)* (2023) [12](#)
46. Yao, Y., Luo, Z., Li, S., Fang, T., Quan, L.: Mvsnet: Depth inference for unstructured multi-view stereo. In: *Proceedings of the European conference on computer vision (ECCV)*. pp. 767–783 (2018) [1](#), [3](#), [6](#), [9](#), [10](#), [11](#), [12](#)
47. Yao, Y., Luo, Z., Li, S., Zhang, J., Ren, Y., Zhou, L., Fang, T., Quan, L.: Blend-edmvs: A large-scale dataset for generalized multi-view stereo networks. *Computer Vision and Pattern Recognition (CVPR)* (2020) [11](#)

48. Yariv, L., Gu, J., Kasten, Y., Lipman, Y.: Volume rendering of neural implicit surfaces. *Advances in Neural Information Processing Systems* **34**, 4805–4815 (2021) [3](#), [9](#), [10](#), [12](#)
49. Yariv, L., Kasten, Y., Moran, D., Galun, M., Atzmon, M., Ronen, B., Lipman, Y.: Multiview neural surface reconstruction by disentangling geometry and appearance. *Advances in Neural Information Processing Systems* **33** (2020) [3](#), [10](#), [12](#)
50. Yu, A., Ye, V., Tancik, M., Kanazawa, A.: pixelnerf: Neural radiance fields from one or few images. In: *Proceedings of the IEEE/CVF Conference on Computer Vision and Pattern Recognition*. pp. 4578–4587 (2021) [3](#), [9](#), [10](#)
51. Yu, Z., Peng, S., Niemeyer, M., Sattler, T., Geiger, A.: Monosdf: Exploring monocular geometric cues for neural implicit surface reconstruction. *Advances in neural information processing systems* **35**, 25018–25032 (2022) [3](#)
52. Zhang, J., Yao, Y., Quan, L.: Learning signed distance field for multi-view surface reconstruction. In: *Proceedings of the IEEE/CVF International Conference on Computer Vision*. pp. 6525–6534 (2021) [3](#), [12](#)
53. Zhou, K., Chen, C., Wang, B., Saputra, M.R.U., Trigoni, N., Markham, A.: Vmloc: Variational fusion for learning-based multimodal camera localization. In: *Proceedings of the AAAI Conference on Artificial Intelligence*. vol. 35, pp. 6165–6173 (2021) [1](#)
54. Zhou, K., Hong, L., Chen, C., Xu, H., Ye, C., Hu, Q., Li, Z.: Devnet: Self-supervised monocular depth learning via density volume construction. In: *European Conference on Computer Vision*. pp. 125–142. Springer (2022) [1](#), [5](#)
55. Zhou, K., Zhong, J.X., Shin, S., Lu, K., Yang, Y., Markham, A., Trigoni, N.: Dynpoint: Dynamic neural point for view synthesis. *Advances in Neural Information Processing Systems* **36** (2024) [8](#)